

© 2022 Optical Society of America. One print or electronic copy may be made for personal use only. Systematic reproduction and distribution, duplication of any material in this paper for a fee or for commercial purposes, or modifications of the content of this paper are prohibited.

Access to this work was provided by the University of Maryland, Baltimore County (UMBC) ScholarWorks@UMBC digital repository on the Maryland Shared Open Access (MD-SOAR) platform.

Please provide feedback

Please support the ScholarWorks@UMBC repository by emailing scholarworks-group@umbc.edu and telling us what having access to this work means to you and why it's important to you. Thank you.

Tradeoff Between the Brillouin and Transverse Mode Instabilities in Yb-doped Fiber Amplifiers

J. T. YOUNG,¹ A. J. GOERS,² D. M. BROWN,² M. L. DENNIS,²
K. LEHR,² C. WEI,¹ C. R. MENYUK,^{2,3} AND J. HU^{1,*}

¹Baylor University, One Bear Place, Waco, TX, 76798

²Johns Hopkins Applied Physics Laboratory, 11100 Johns Hopkins Road, Laurel, MD 20723

³Permanent address: University of Maryland Baltimore County, 1000 Hilltop Circle, Baltimore, MD 21270

*jonathan_hu@baylor.edu

Abstract:

The Brillouin instability (BI) due to stimulated Brillouin scattering (SBS) and the transverse (thermal) mode instability (TMI) due to stimulated thermal Rayleigh scattering (STRS) limit the achievable power in high-power lasers and amplifiers. The pump power threshold for BI increases as the core diameter increases, but the threshold for TMI may decrease as the core diameter increases. In this paper, we use a multi-time-scale approach to simultaneously model BI and TMI, which gives us the ability to find the fiber diameter with the highest power threshold. We formulate the equations to compare the thresholds of the combined and individual TMI and BI models. At the pump power threshold, and below there is a negligible difference between the full and individual models, as BI and TMI are not strong enough to interact with each other. The highest pump threshold occurs at the optimal core size of $43\ \mu\text{m}$ for the simple double-clad geometry that we considered. We found that both effects contribute equally to the threshold, and the full BI and TMI model yields a similar threshold as the BI or TMI model alone. However, once the reflectivity is sufficiently large, we find in the full BI and TMI model that BI may trigger TMI and reduce the TMI threshold to a value lower than is predicted in simulations with TMI alone. This result cannot be predicted by models that consider BI and TMI separately. Our approach can be extended to more complex geometries and used for their optimization.

© 2022 Optical Society of America under the terms of the [OSA Open Access Publishing Agreement](#)

1. Introduction

Stimulated Brillouin Scattering (SBS) and stimulated thermal Rayleigh scattering (STRS) can lead respectively to the Brillouin instability (BI) and the transverse mode instability (TMI) which limit the output power in optical fibers [1–3]. For BI, a forward-propagating optical mode couples to an acoustic mode and the same optical mode propagating in the backward direction (Stokes mode) [4–10]. For TMI, an optical mode couples to a higher-order mode (HOM) that has nearly the same frequency [11–17] and a transverse thermal mode. In both cases, the instability is characterized by exponential growth that leads to a sharp pump power threshold, beyond which significant power is transferred to modes other than the forward-propagating fundamental mode. Both instabilities impose limits on the output power of Yb³⁺-doped fiber amplifiers, and the interaction between these two instabilities is not well understood. Also, the limits that they impose depend differently on the fiber core diameter. As the fiber core diameter increases, all else being equal, the BI threshold increases because the optical intensity decreases for a fixed power. However, as the fiber core diameter increases, the TMI threshold may decrease due to an increased interaction between the fundamental mode and the HOM. The wavenumbers of the HOMs at the same frequency come closer to the wavenumber of the fundamental mode, easing the coupling condition for the thermal mode so that TMI is more easily triggered. Thus, a tradeoff typically exists between BI and TMI as the diameter increases.

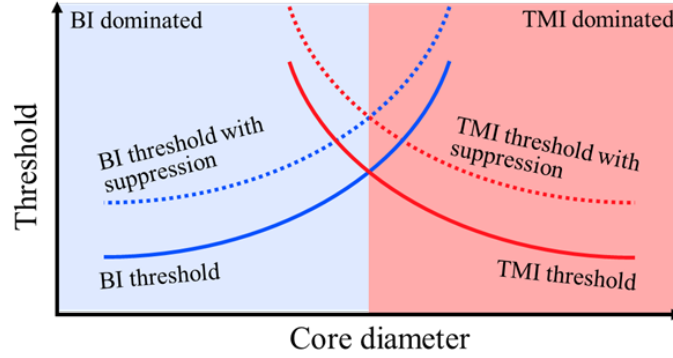


Fig. 1. Illustration of the tradeoff between the Brillouin instability and the transverse mode instability.

Figure 1 illustrates schematically the dependence of the pump power threshold for the individual BI and TMI effects. Using mitigation techniques for BI such as phase modulation [7, 8] will likely decrease the core diameter where both BI and TMI play a roughly equal role in limiting the pump power threshold. On the other hand, mitigation techniques for TMI, such as fiber bending [18, 19], fiber tapering [20], gain filtering [21], use of specially designed photonic crystal fibers [22], and detuning of the pump and signal wavelengths [23, 24] will increase the core diameter at which both BI and TMI play an equal role in limiting the pump power threshold. Thus, it is typically the case that the maximum power threshold is obtained for designs in which BI and TMI play a roughly equal role in limiting the power. Hence, it is critical to develop a model that can study the interaction between BI and TMI.

In this paper, we determine the optimal fiber core diameter for an Yb^{3+} -doped fiber amplifier with a simple double-clad geometry. Previous research has examined the tradeoff among BI and TMI [25–27]. Here, we formulate the full BI and TMI model and compare this full model to their respective individual models at different pump powers in order to highlight the differences between them. Simultaneously modeling BI and TMI is challenging because the time scales on which they develop are different. BI, which is associated with acoustic phonons, has a characteristic time scale on the order of nanoseconds, while TMI, which is associated with thermal diffusion, has a time scale on the order of milliseconds. This large difference in time scales implies that a multi-time-scale approach must be used. For that reason, almost all work to date has considered these two instabilities separately. In this paper, we describe a multi-time-scale approach that allows us to simultaneously model BI and TMI. This approach can be extended to more complex geometries in which the overlap of the fundamental mode with the acoustic mode, the thermal mode, and HOMs is minimized. That in turn will make it possible to optimize the optical fiber designs to increase the threshold powers.

2. Modeling scheme

Figure 2 shows the time discretization scheme for the simulation. Between two TMI iteration steps, which are separated by a time on the order of 1 ms, we take many small time steps, which are separated by a time on the order of 1 ns in order to take BI into consideration. Once the modes have reached steady state on the BI time scale, we jump to the next TMI step. For simplicity, we keep the z -step the same when modeling both BI and TMI. At a minimum, three optical modes representing the forward fundamental mode, forward HOM, and backward fundamental Stokes mode, one thermal mode, and one acoustic mode must be considered for the full BI and TMI

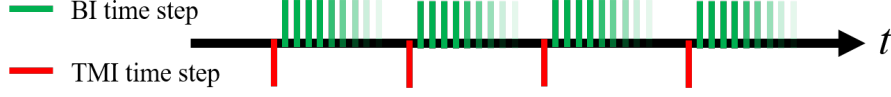


Fig. 2. Time step scheme. After each TMI time step, a series of BI steps are taken until the fundamental mode and Stokes mode reach steady state.

simulation.

Figure 3 shows an illustration of all the modes that we keep in our model. To model TMI, we include the fundamental mode and one HOM. Most theoretical studies of TMI to date focus on evolution after the onset of TMI when the fundamental mode is significantly depleted. These studies are of little interest for most applications, including applications to high-energy laser beam production, because once forward propagating HOMs have a total power that exceeds about 1% of the output power, the beam quality is unacceptably degraded [12]. Hence, only one HOM is needed to determine the onset of TMI. In BI modeling, we only account for the backward-propagating Stokes mode that is generated by the fundamental mode since we only consider cases where the HOM does not make up the majority of the output power at or below the threshold.

We must also clarify the nomenclature that we use for the different modes. In the TMI literature, it is usual to refer to the optical modes as the pump mode, fundamental mode, and HOM. However, in the BI literature, it is usual to refer to the optical modes as the pump mode and Stokes mode. Although, there is no ambiguity for the Stokes mode, the pump mode in the BI literature corresponds to the fundamental mode in the TMI literature. In this paper, we will refer to the mode that pumps the laser amplifier as the pump mode, the mode that is amplified as the fundamental mode, the optical mode generated by TMI as the HOM, and the optical mode generated by BI as the Stokes mode.

3. Model for BI and TMI

In much of the current literature, the equations that describe BI use an electric field amplitude for each mode that has been normalized so that the power for mode l , P_l , is given by $P_l = (1/2)nc\epsilon_0 A_{\text{eff}} |E_l|^2$, where A_{eff} is the effective area [28]. This choice of normalization is possible since both the forward-propagating fundamental mode and the backward-propagating

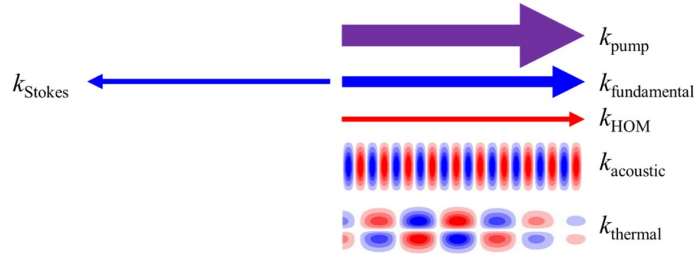


Fig. 3. Illustration of the modes for the BI and TMI simulations. The pump (k_{pump}), fundamental mode ($k_{\text{fundamental}}$), and HOM (k_{HOM}) propagate in the positive z -direction and have positive wavenumbers. The Stokes mode (k_{Stokes}) propagates backwards and has a negative wavenumber. We represent the density oscillation for k_{acoustic} , and the oscillation in the transverse temperature flow for k_{thermal} .

Stokes mode have the same transverse mode profile. In the case of TMI, this normalization is no longer possible since the fundamental mode and the HOM have different mode profiles. Moreover, as Kobayakov et al. [29] have pointed out, this choice is of limited utility since the definition of A_{eff} becomes ambiguous, and it is important to correctly account for the overlap between the optical and acoustic modes when computing gain coefficients. For that reason, we will consistently use field amplitudes A_l that are normalized so that $P_l = (1/2)cn\epsilon_0|A_l|^2$ where $A_l = E_l(A_{\text{eff},l})^{1/2}$. The amplitudes of the fundamental mode, HOM, and Stokes mode will be denoted as A_F , A_H , and A_S , respectively.

In this paper, we will focus on fibers with a simple geometry in which the interacting modes are all LP modes in a single polarization so that we may write the electric field for mode l as [30]

$$\mathbf{E}_l(\mathbf{r}_\perp, z, t) = \hat{\mathbf{x}} \frac{1}{2} [A_l(z, t) \mathcal{E}_l(\mathbf{r}_\perp) \exp(i\beta z - i\omega t) + \text{c.c.}], \quad (1)$$

where $\hat{\mathbf{x}}$ denotes the mode polarization direction, A_l ($l=F, H$, or S) denotes the mode amplitude, and $\mathcal{E}_l(\mathbf{r}_\perp)$ is the transverse mode profile, normalized so that $\int d^2\mathbf{r}_\perp |\mathcal{E}_l(\mathbf{r}_\perp)|^2 = 1$. We note that $\mathcal{E}_S(\mathbf{r}_\perp) = \mathcal{E}_F(\mathbf{r}_\perp)$. We then find that the equations describing TMI may be written as [31]

$$\begin{aligned} \frac{dA_F}{dz} &= C_{FF}A_F + C_{FH}A_H, \\ \frac{dA_H}{dz} &= C_{HH}A_H + C_{HF}A_F, \end{aligned} \quad (2)$$

where

$$\begin{aligned} C_{FF} &= \frac{i\omega^2}{\beta c^2} n_0 \int d^2\mathbf{r}_\perp |\mathcal{E}_F|^2 \Delta n_0, \\ C_{FH} &= \frac{i\omega^2}{\beta c^2} n_0 \int d^2\mathbf{r}_\perp \mathcal{E}_F^* \mathcal{E}_H \Delta n_+, \\ C_{HF} &= \frac{i\omega^2}{\beta c^2} n_0 \int d^2\mathbf{r}_\perp \mathcal{E}_F \mathcal{E}_H^* \Delta n_-, \\ C_{HH} &= \frac{i\omega^2}{\beta c^2} n_0 \int d^2\mathbf{r}_\perp |\mathcal{E}_H|^2 \Delta n_0. \end{aligned} \quad (3)$$

Here, the quantities C_{FF} , C_{FH} , C_{HF} , and C_{HH} are optical gains or losses influenced by TMI. These gains or losses do not vary on the BI's nanosecond time scale since they are only dependent on the change in refractive index and temperature, which vary on the order of milliseconds. In Eq. (3), we are using the phase-matched model [31], in which we set

$$\Delta n(z, t) = \Delta n_0(z, t) + \frac{1}{2} [\Delta n_+(z, t) \exp(i\Delta\beta z) + \Delta n_-(z, t) \exp(-i\Delta\beta z)], \quad (4)$$

where $\Delta n(z, t)$ is the total change in the refractive index due to TMI and $\Delta\beta = \beta_H - \beta_F$ represents the difference in propagation constants of the fundamental mode and HOM. The basic assumption of the phase-matched model is that all quantities have a component that varies slowly along the fiber compared to the beat length $2\pi/\Delta\beta$ and a component that oscillates at the beat length period, whose complex amplitude varies slowly compared to the beat length. In the phase-matched model, we ignore contributions to $\Delta n(z, t)$ from higher harmonics of $\Delta\beta$. It was previously shown that this approximation greatly speeds the computational calculations with no loss in accuracy [31] since the contributions of higher harmonics that are proportional to $\exp(im\Delta\beta z)$ with $m > 1$ are negligible. Conversely, we have $|\Delta\beta| \ll \beta_H$, $\beta_F \approx \beta$.

We model BI [4, 7] including the contributions from TMI using the equations

$$\begin{aligned}
\frac{\partial A_F}{\partial z} + \frac{1}{v_g} \frac{\partial A_F}{\partial t} &= C_{FF}A_F + C_{FH}A_H + i\kappa A_S \rho, \\
\frac{\partial A_H}{\partial z} + \frac{1}{v_g} \frac{\partial A_H}{\partial t} &= C_{HH}A_H + C_{HF}A_F, \\
-\frac{\partial A_S}{\partial z} + \frac{1}{v_g} \frac{\partial A_S}{\partial t} &= C_{FF}A_S + i\kappa A_F \rho^*, \\
\frac{\partial \rho}{\partial t} + \pi \Delta v_B \rho &= i \frac{\Lambda}{A_{\text{eff},F}} A_F A_S^* + f,
\end{aligned} \tag{5}$$

where $\rho(z, t)$ is the acoustic wave density, κ and Λ are the optical and acoustic coupling parameters [4], Δv_B is the Brillouin linewidth, and $A_{\text{eff},F}$ is the effective area for the fundamental mode and Stokes mode. The parameters C_{FF} , C_{FH} , C_{HF} , and C_{HH} are the TMI contributions to the evolution of different fields according to Eq. (3). The quantity v_g represents the group velocity of the fundamental mode. Since the frequency difference between the fundamental mode and HOM is on the order of kHz, we assume that the difference in group velocities between the two modes is negligible. Since the Stokes mode and fundamental mode share nearly the same transverse mode profile, and the frequency shift between them is only on the order of tens of GHz [32, 33], we assume that gain and group velocity for the Stokes mode is the same as for the fundamental mode. We assume that the acoustic noise source $f(z, t)$ is white thermal noise [4, 34], which is delta-correlated such that

$$\langle f(z, t) f^*(z', t') \rangle = Q \delta(z - z') \delta(t - t'). \tag{6}$$

Here, the coefficient Q is the phonon strength parameter and is expressed as

$$Q = \frac{4\pi k T \rho_0 \Delta v_B}{v^2 A_{\text{eff}}}, \tag{7}$$

where k is the Boltzmann constant, T is the temperature along the fiber, and v is the speed of sound through the material.

To model the heat flow in the fiber, we write

$$\rho_0 C \frac{\partial T_0}{\partial t} + \kappa \nabla_{\perp}^2 T_0 = Q_0, \quad \rho_0 C \frac{\partial T_{\pm}}{\partial t} + \kappa \nabla_{\perp}^2 T_{\pm} = Q_{\pm}, \tag{8}$$

where, consistent with the phase-matched model [31], we write the temperature as $T = T_0 + (1/2)[T_+ \exp(i\Delta\beta z) + T_- \exp(-i\Delta\beta z)]$, and we assume that T_0 , T_+ , and $T_- = T_+^*$ all vary slowly along z compared to the beat length $2\pi/\Delta\beta$. We similarly write $Q = Q_0 + (1/2)[Q_+ \exp(i\Delta\beta z) + Q_- \exp(-i\Delta\beta z)]$, where Q_0 , Q_+ , and $Q_- = Q_+^*$ all vary slowly compared to the beat length. More details on the phase-matched model that we use here can be found in [31].

When including BI in our model, we only consider the Stokes mode generated by the fundamental mode. Since we focus on the power threshold, the power in the HOM is low (1%) compared to the power in the fundamental mode. Any Stokes light generated from the HOM would be orders of magnitude smaller than the Stokes light generated from the fundamental mode and would make a negligible contribution to the reflectivity. Also, we only consider the forward propagating fundamental mode as any backward propagating fundamental modes would be small at or below the threshold.

Since the gain and temperature profiles vary on the scale of milliseconds, they may be treated as time-independent in each BI step, which occurs on the scale of nanoseconds. This implies that C_{FF} , C_{FH} , C_{HF} , and C_{HH} are fixed with respect to the BI time step. After each TMI step, we solve

the BI equations, taking time steps on the order of nanoseconds until a steady state is reached. When modeling the BI portion of the simulation, we set the temporal step size $\Delta t = \Delta z / v_g$, where Δz is the step size in the longitudinal direction [4, 7]. In each BI time step, we first propagate the fundamental mode and the HOM in the forward direction. Then, we propagate the Stokes mode in the backward direction. This relaxation algorithm is commonly used for two-point boundary value problems [35], where $A_F(z = 0, t) = [2P_{F0}/(cn\epsilon_0)]^{1/2}$, $A_S(z = L, t) = 0$, and P_{F0} is the input optical power of the signal in fundamental mode. At the beginning of the simulation, we assume that $A_S(z, t < 0) = 0$. We propagate the optical fields for 40 fiber transient times to ensure that the power reaches a steady state, and we then take a statistical average of the Stokes mode at the front of the fiber and the power at the fiber output for an additional 40 fiber transient times. The transient time equals L/v_g , which is 7.7 ns in this case. Because we use a noise source to seed the BI process, we must take a statistical average, which better reflects experimental measurement.

Table 1 shows the fiber parameters used for the simulation [4, 15]. The ratio of cladding diameter, d_{clad} , to core diameter, d_{core} , is fixed at 5 to ensure that the total signal gain is the same within 5% for all core sizes when the pump power is below threshold. The overall goal of our simulation is to vary the core diameter to find the highest threshold when both BI and TMI are considered. Consistent with prior work [15, 31], we assume that the frequency difference between the fundamental mode and the HOM is 1 kHz. We consider a numerical aperture of 0.03, which is consistent with the numerical apertures reported in experiments [36–38]. We use a 10th-order super-Gaussian profile for the rare-earth doping concentration in the fiber cross-section [39].

In this paper, we focus on the contribution to TMI due to the quantum defect heating [13–15]. It has been shown that photodarkening can also contribute to TMI [23, 40]. Photodarkening contributes to the thermally induced index grating coherently with quantum defect heating [17]. Hence, the heat source term and absorption term from photodarkening [23] could in principle be added to the phase-matched model for TMI [31].

Table 1. Simulation Parameters

| | | | | | |
|--------------------|-------------------------|------------------------------------|----------------------|---------------------------|------------------------------------|
| Fiber length | L | 1.6 m | Doping concentration | N_0 | $6 \times 10^{25} \text{ m}^{-3}$ |
| Core index | n_{core} | 1.45031 | Brillouin linewidth | $\Delta\nu_B$ | 57 MHz |
| Numerical aperture | $N.A.$ | 0.03 | Heat lifetime | τ | 0.85 ms |
| Signal power | P_{sig} | 30 W | Pump wavelength | λ_{pump} | 977 nm |
| HOM seed power | P_{HOM} | 3 mW | Signal wavelength | λ_{signal} | 1064 nm |
| Pump emission | $\sigma_p^{(e)}$ | $1.87 \times 10^{-27} \text{ m}^2$ | Pump absorption | $\sigma_p^{(a)}$ | $1.53 \times 10^{-24} \text{ m}^2$ |
| Signal emission | $\sigma_s^{(e)}$ | $6 \times 10^{-27} \text{ m}^2$ | Signal absorption | $\sigma_s^{(a)}$ | $3.58 \times 10^{-25} \text{ m}^2$ |
| z step | Δz | $8 \times 10^{-5} \text{ m}$ | Density | ρ_0 | 2200 kg/m^3 |
| t step, TMI | Δt_{TMI} | 20 μs | Heat capacity | C | 703 J/(kg – K) |
| t step, BI | Δt_{BI} | 0.774 ps | Thermal conductivity | κ | 1.38 W/(m – K) |
| Transverse step | $\Delta x, \Delta y$ | 2 μm | Initial temperature | T | 300 K |

4. BI and TMI threshold at core diameters of 30 and 45 μm

When we refer to the threshold, we are always referring to the pump power threshold that is limited by either BI or TMI. We define the threshold for BI, $P_{\text{pump, BI}}$, as the input pump power at which the reflectivity defined as $\rho_S = \overline{P_S(z=0)} / [\overline{P_F(z=L)} + \overline{P_S(z=0)}]$ reaches 1%, where the overline indicates an average over the 40 transient fiber times $t_f = Ln/c$, as described in the previous section. This definition of reflectivity is used in the gain fiber so that the reflectivity represents the ratio of the reflected power relative to the amount of total output power that is reflected, and the lower and upper bounds of ρ_S in this definition are 0 and 1, which is consistent with the definition of the HOM content. To ensure that the power reaches a steady state due to TMI, we also average the reflectivity in the full model over the last 50 TMI steps. We define the threshold for TMI, $P_{\text{pump, TMI}}$, as the input pump power at which the HOM content defined as $\rho_H = \max\{P_H(z=L) / [P_F(z=L) + P_H(z=L)]\}$ reaches 1% [31]. We write the maximum in the definition since the impact of TMI is determined by this maximum value [15, 31]. When we consider BI and TMI together, the threshold, $P_{\text{pump, full}}$, is defined as the pump power at which the maximum of the reflectivity ρ_S or the HOM content ρ_H reaches 1%. We study the thresholds for BI and TMI using the full model described in the previous section for core diameters of 30 and 45 μm . The dashed blue and dotted red curves in Fig. 4 show reflectivity, ρ_S , and the HOM

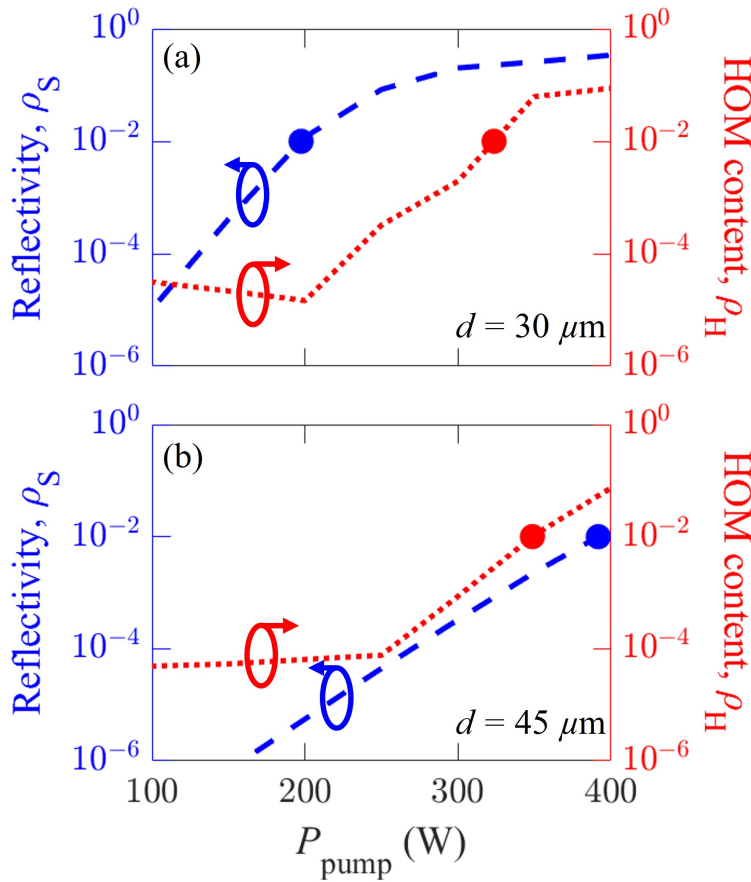


Fig. 4. Reflectivity ρ_S due to BI and the HOM content ρ_H due to TMI as a function of pump power for a core diameter of (a) $d = 30 \mu\text{m}$ and (b) $d = 45 \mu\text{m}$. The results here are obtained using the full model that includes both BI and TMI.

content, ρ_H , respectively, as a function of pump power. For fibers with the smaller core diameter of $30\ \mu\text{m}$, shown in Fig. 4(a), the pump power is 197 W when the reflectivity ρ_S reaches 1%, and the pump power is 323 W when the HOM content ρ_H reaches 1%. In this case, BI plays a more important role and reaches threshold at a lower pump power since the relatively small core size increases the intensity. By contrast, for fibers with the larger core diameter of $45\ \mu\text{m}$, the pump power is 391 W when the reflectivity ρ_S reaches 1%, and the pump power is 348 W when the HOM content ρ_H reaches 1%. In this case, TMI is the dominant effect that limits the pump power threshold due to a stronger coupling between the fundamental mode and the HOM. When TMI is the limiting nonlinear effect, decreasing the core diameter improves the TMI threshold.

5. BI and TMI thresholds as a function of core diameter

In Fig. 5(a), the solid green curve shows the threshold $P_{\text{pump,full}}$, which is the power, including the effects of both BI and TMI. We also show P_{fund} , which is the output power for the fundamental mode at the pump power threshold $P_{\text{pump,full}}$. As explained in the previous section, increasing the diameter increases the modal area and lowers the intensity, which helps to improve the BI threshold. However, further increasing the diameter eventually increases the impact of the HOM in our study, which lowers the TMI threshold. The cutoff diameter in our study for the HOM is at $27.2\ \mu\text{m}$. Decreasing the core diameter to values near the cutoff of the HOM will cause the HOM to be less confined and greatly increase the TMI threshold. In Fig. 5(b), the dashed and dotted green curves show the reflectivity ρ_S and the HOM content ρ_H , respectively, for the full model at the corresponding pump power indicated by the green curve in Fig. 5(a). Since our definition of threshold is when either the reflectivity or the HOM content reaches 1%, the curves in Fig. 5(b) will be capped at 1%. Figure 5(b) clearly indicates the limiting effect on the

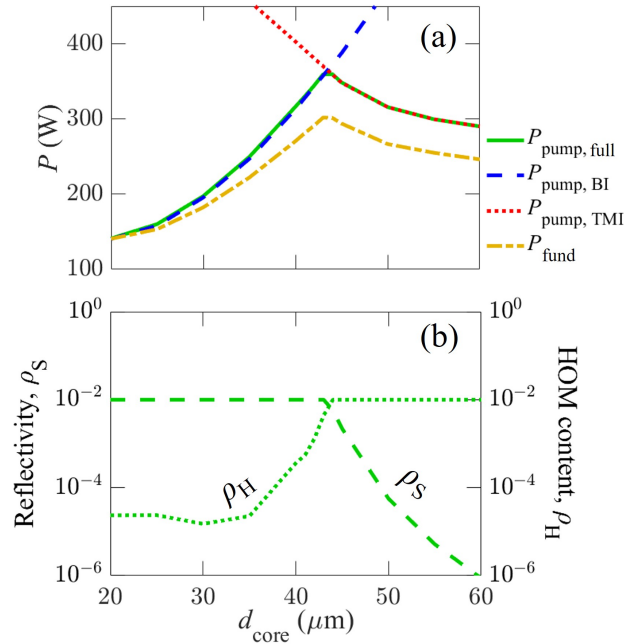


Fig. 5. (a) Pump power threshold when we consider BI and TMI altogether or BI and TMI separately. The fundamental mode power P_{fund} shows the output power for the fundamental mode at the pump power threshold $P_{\text{pump,full}}$. (b) Reflectivity ρ_S and HOM content ρ_H for the full model at the corresponding pump power threshold, $P_{\text{pump,full}}$, indicated by the green curve in (a).

instability corresponding to the pump power threshold curve in Fig. 5(a). The core diameter of $43\text{ }\mu\text{m}$ yields the highest threshold; at that diameter the threshold contributions due to BI and TMI are equal. The dash-dotted orange curve in Fig. 5(a) shows the output power at the pump power threshold, which indicates the maximum output power at the optimal core diameter of $43\text{ }\mu\text{m}$.

In Fig. 5(a), the dotted red curve shows the threshold power, $P_{\text{pump,TMI}}$, when only TMI is present. The dashed blue curve shows the threshold power, $P_{\text{pump,BI}}$, when only BI is present. At a small diameter of $20\text{ }\mu\text{m}$, the full model agrees with the BI only model, that only includes BI, as there is a negligible influence on the pump power threshold due to TMI. At a large diameter of $60\text{ }\mu\text{m}$, the threshold for the full model agrees with the threshold for the TMI only model, the model that only includes TMI, as BI makes a negligible contribution to the pump power threshold.

6. Comparison of the individual and full models

Figure 4 also shows that when the full BI and TMI model is considered, the TMI threshold for a core diameter of $30\text{ }\mu\text{m}$ is lower than the threshold for a core diameter of $45\text{ }\mu\text{m}$. This result is contrary to the expectation that decreasing the core diameter should increase the TMI threshold. In Fig. 4(a), we see that after the BI threshold is reached at 197 W , there is significant reflection of the output power. We observe that the onset of TMI may occur at a lower-than-normal pump power when the reflectivity due to BI is sufficiently high and the pump power is above the BI threshold so the reflectivity is greater than 1%.

Next, we study when BI will trigger TMI. Figure 6 shows the full model reflectivity and HOM content compared to the HOM content from the TMI only model as a function of pump power. The core diameter is $30\text{ }\mu\text{m}$. The dashed blue and dotted red curves are replotted from Fig. 4(a) so that the comparison may be easily made. The solid green curve shows the HOM content from the TMI only model. The dotted black horizontal line in Fig. 6 marks the 1% threshold criterion. Figure 6 shows that when the pump power is under 200 W , the reflectivity is low, and there is a negligible difference between the HOM content predicted by the TMI only model and the full model. However, further increasing the pump power past 200 W yields an increase in reflectivity that then triggers TMI in the full model. The TMI threshold with the full model is at a pump power of 323 W compared to the TMI only threshold of 946 W .

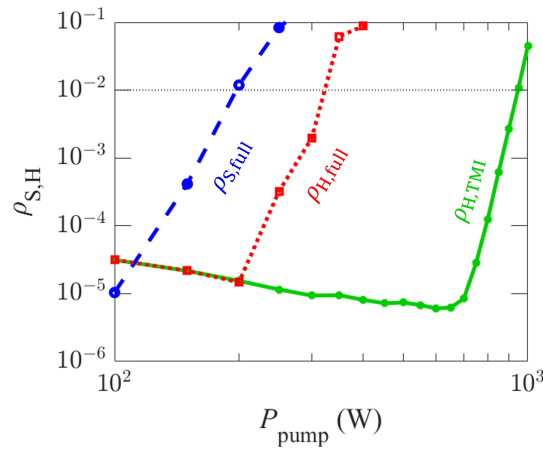


Fig. 6. Reflectivity and HOM content from the full model and the TMI only model as a function of pump power. The core diameter is $30\text{ }\mu\text{m}$.

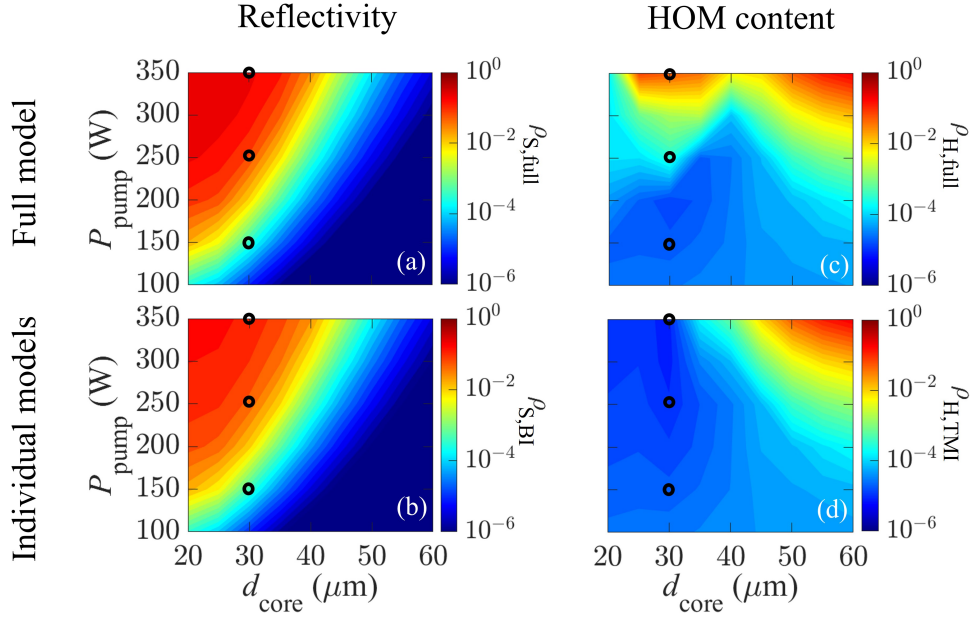


Fig. 7. (a) Reflectivity from the full model, (b) reflectivity from the BI only model, (c) HOM content from the full model, and (d) HOM content from the TMI only model as a function of pump power and core diameter. Black circles in (a)–(d) show pump powers of 150, 250, and 350 W at a core diameter of $30 \mu\text{m}$.

In this example, the onset of BI at 1% does not trigger TMI, but rather TMI is triggered by BI when the reflectivity reaches about 10%. If there is significant reflectivity, much greater than the 1% used to denote the onset of BI, the interaction between the Stokes and fundamental mode causes the fundamental mode to fluctuate stochastically along the fiber. Rather than seeding the HOM directly, these fluctuations may make it possible for the fundamental mode and the HOM to interact. This result is consistent with experiments of Lee et al. [41] who found that stimulated Brillouin scattering may induce TMI and that the TMI threshold closely follows the BI threshold. This behavior is not captured by previous models that consider TMI or BI separately.

To gain a better understanding of the interaction between the TMI and BI, we now compare the full model and individual models at different power levels so that any differences between

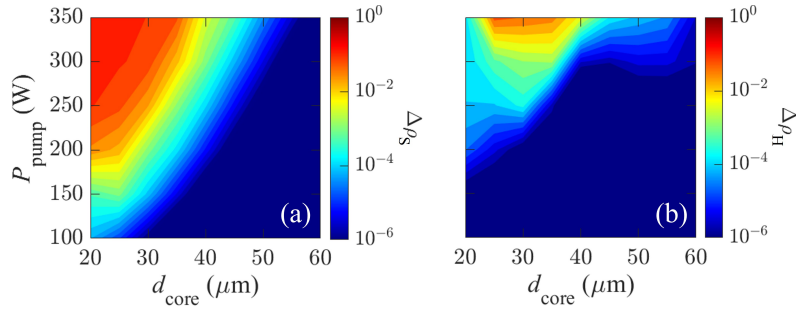


Fig. 8. Absolute value of the difference in the predicted (a) reflectivity and (b) HOM content between the full and individual models.

them may be distinguished. Figures 7(a)–(d) show the full model reflectivity $\rho_{S,\text{full}}$, BI only reflectivity $\rho_{S,\text{BI}}$, full model HOM content $\rho_{H,\text{full}}$, and TMI only HOM content, $\rho_{H,\text{TMI}}$ as a function of pump power and core diameter. In Fig. 7(a), the reflectivity increases as the power increases or the core diameter decreases.

To further understand the difference in predicted reflectivity and HOM content between the individual BI and TMI models to the full model, we show the difference in predicted reflectivity $\Delta\rho_S = |\rho_{S,\text{BI}} - \rho_{S,\text{full}}|$ and HOM content $\Delta\rho_H = |\rho_{H,\text{TMI}} - \rho_{S,\text{full}}|$, between the full model and individual models in Fig. 8. The temperature in the full model increases due to the quantum defect, which can lead to a difference in the predicted reflectivity values between the full model and the BI only model, as shown in Fig. 8(a). Figure 8(b) shows that when the full model is under the BI threshold, there is a negligible difference in the predicted HOM content between the full model and the TMI only model. However, once there is significant reflectivity at $d_{\text{core}} = 30 \mu\text{m}$ and $P_{\text{pump}} = 350 \text{ W}$, the HOM content predicted by the full model differs from the HOM content predicted by the TMI only model.

To compare the HOM content that is predicted by the different models, we study the evolution of the reflectivity and the HOM content as a function of time for the three regions marked with circles in Fig. 7. Figures 9(a)–(c) show the reflectivity and the HOM content for pump

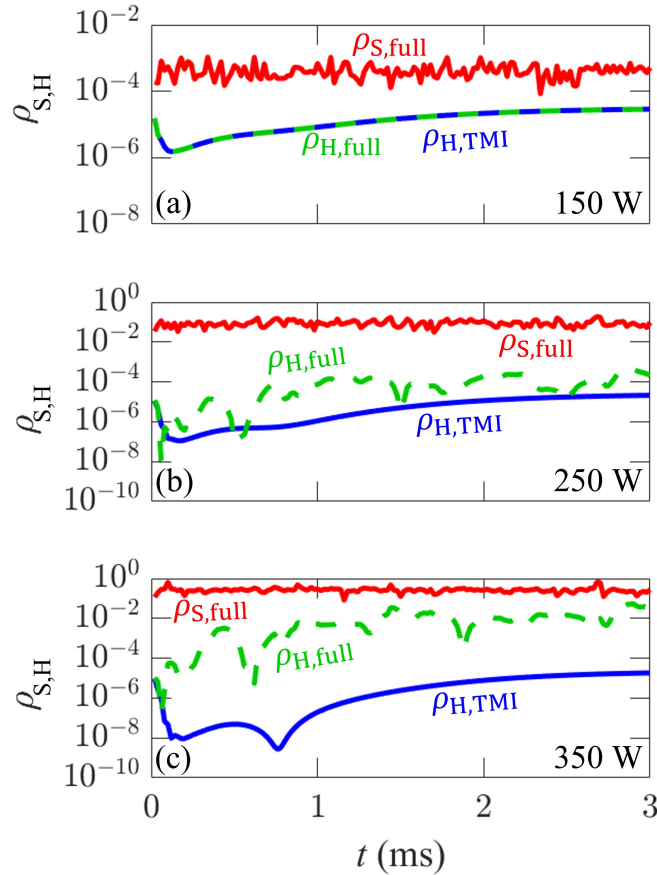


Fig. 9. Reflectivity and HOM content as a function of time for pump powers of (a) 150 W, (b) 250 W, and (c) 350 W with a core diameter of $30 \mu\text{m}$.

powers of 150, 250, and 350 W, respectively, as a function of time. The core diameter is 30 μm . The solid blue, dashed green, and solid red curves represent the HOM content from a TMI only simulation $\rho_{\text{H,TMI}}$, HOM content for the full model $\rho_{\text{H,full}}$, and reflectivity from the full model $\rho_{\text{S,full}}$, respectively. When the pump power is 150 W, the averaged reflectivity is 0.043% which is under the BI threshold. The HOM content predicted by the full model and by the TMI only model are nearly identical. In this case, adding BI in the model does not have any impact on TMI. At a pump power of 250 W, the averaged reflectivity is near 8.9%. Both the TMI only model and full model lead to a small HOM content below 1%. The difference in the peak HOM content is also small. Hence, around the BI threshold, the interaction between BI and TMI is not significant, as shown in Fig. 9(b). However, when the pump power increases to 350 W, the averaged reflectivity reaches 27%. The higher reflectivity leads to amplitude modulation of the signal and triggers TMI, as shown in Fig. 9(c). In this case, the large BI leads to significant power transfer between the fundamental mode and the Stokes mode. Hence, there is a substantial difference in the time evolution of the HOM contents between the full model and the TMI only model, which leads to different contours in Figs. 7(c) and (d).

7. Conclusions

BI and TMI have been modeled separately in the past, but including both effects in one simulation is necessary to determine when and how they interact particularly since both effects have roughly equal magnitudes at the optimal operating points in the parameter space. We formulate the equations to model both BI and TMI in a single simulation. For the system model and parameters that we considered, the optimal core diameter with a maximum power threshold is around 43 μm . For small core sizes less than the optimal core diameter of 43 μm , BI dominates and TMI plays little role in limiting the pump power threshold. For core sizes that are greater than 43 μm , the BI effect is negligible, and the full model with both BI and TMI yields a similar threshold as the threshold for TMI alone. The difference between the full model and individual model pump power thresholds is negligible in this case, as BI and TMI are not strong enough to interact with each other. At large pump powers and small core diameters, where the reflectivity is large, BI may trigger TMI due to modulation of the power in the fundamental mode, so that the TMI threshold is significantly lower than is the case when modeling TMI alone.

Combining both BI and TMI in a single simulation makes it possible to simultaneously optimize the fiber design to minimize both effects and yield the highest power thresholds.

Disclosures. The authors declare no conflicts of interest.

Data availability. Data underlying the results presented in this paper are not publicly available at this time but may be obtained from the authors upon reasonable request.

References

1. C. Jauregui, J. Limpert and A. Tünnermann, "High-power fibre lasers," *Nature Photon* **7**, 861–867 (2013).
2. M. N. Zervas and C. A. Codemard, "High power fiber lasers: A review," *IEEE J. Sel. Topics Quantum Electron* **20**(5), 219–241 (2014).
3. D. J. Richardson, J. Nilsson, and W. A. Clarkson, "High power fiber lasers: current status and future perspectives [Invited]," *J. Opt. Soc. Am. B* **27**(11), B63–B92 (2010).
4. C. E. Mungan, S. D. Rogers, N. Satyan, and J. O. White, "Time-dependent modeling of Brillouin scattering in optical fibers excited by a chirped laser diode," *J. Sel. Topics Quantum Electron* **48**(12), 1542–1546 (2012).
5. E. Petersen, Z. Y. Yang, N. Satyan, A. Vasilyev, G. Rakuljic, A. Yariv, J. O. White, "Stimulated Brillouin scattering suppression with a chirped laser seed: comparison of dynamical model to experimental data," *J. Sel. Topics Quantum Electron* **49**(12), 1040–1044 (2013).
6. A. David and M. Horowitz, "Low-frequency transmitted intensity noise induced by stimulated Brillouin scattering in optical fibers," *Opt. Express* **19**(12), 11792–11803 (2011).
7. C. Zeringue, I. Dajani, S. Naderi, G. T. Moore, and C. Robin, "A theoretical study of transient stimulated Brillouin scattering in optical fibers seeded with phase-modulated light," *Opt. Express* **20**(19), 21196–21213 (2012).
8. J. O. White, J. T. Young, C. Wei, J. Hu, and C. R. Menyuk, "Seeding fiber amplifiers for high SBS thresholds and compact spectra," *Opt. Express*, **27**(3), 2962–2974 (2019).

9. B. M. Cannon, D. M. Brown, M. J. Mayr, M. L. Dennis, W. E. Torruellas, J. O. White, "High energy fiber laser amplifier with reduced optical linewidth," US patent 20180269645A1 (Sep. 20, 2018).
10. D. Brown, M. Dennis, and W. Torruellas, "Improved phase modulation for SBS mitigation in kW-class fiber amplifiers," presented at the SPIE Photon. West, San Francisco, CA, USA, Jan. 2011.
11. C. Jauregui, T. Eidam, J. Limpert, and A. Tünnermann, "Impact of modal interference on beam quality of high-power amplifiers," *Opt. Express* **19**(4), 3258–3271 (2011).
12. T. Eidam, C. Wirth, C. Jauregui, F. Stutzki, F. Jansen, H.-J. Otto, O. Schmidt, T. Schreiber, J. Limpert, A. Tünnermann, "Experimental observations of the threshold-like onset of mode instabilities in high power fiber amplifiers," *Opt. Express* **19**(14), 13218–13224 (2011).
13. A. V. Smith and J. J. Smith, "Mode instability in high-power fiber amplifiers," *Opt. Express* **19**(11), 10180–10192 (2011).
14. B. Ward, C. Robin, and I. Dajani, "Origin of thermal mode instabilities in large mode area fiber amplifiers," *Opt. Express* **20**(10), 11407–11422 (2012).
15. S. Naderi, I. Dajani, T. Madden, and C. Robin, "Investigations of modal instabilities in fiber amplifiers through detailed numerical simulations," *Opt. Express* **21**(13), 16111–16129 (2013).
16. K. R. Hansen, T. T. Alkeskjold, J. Broeng, and J. Lægsgaard, "Theoretical analysis of mode instability in high-power amplifiers," *Opt. Express* **21**(2), 1944–1971 (2013).
17. C. Jauregui, C. Stihler, and J. Limpert, "Transverse mode instability," *Adv. Opt. Photonics* **12**(2), 429–484 (2021).
18. F. Beier, C. Hupel, J. Nold, S. Kuhn, S. Hein, J. Ihring, B. Sattler, N. Haarlamert, T. Schreiber, R. Eberhardt, and A. Tünnermann, "Narrow linewidth, single mode 3 kW average power from a directly diode pumped ytterbium-doped low NA fiber amplifier," *Opt. Express* **24**(6), 6011–6020 (2016).
19. R. Tao, R. Su, P. Ma, X. Wang, and P. Zhou, "Suppressing mode instabilities by optimizing the fiber coiling methods," *Laser Phys. Lett.* **14**, 025101 (2017).
20. L. Zeng, X. Xi, Y. Ye, X. Lin, X. Wang, J. Li, C. Shi, B. Yang, H. Zhang, P. Wang, P. Zhou, X. Xu, "A novel fiber laser oscillator employing saddle-shaped core ytterbium-doped fiber," *Applied Physics B* **126**, 185 (2020).
21. J. P. Leidner and J. R. Marcianite, "Three fiber designs for mitigating thermal mode instability in high-power fiber amplifiers," *Opt. Express* **28**(19), 28502–28516 (2020).
22. F. Kong, G. Gu, T. W. Hawkins, M. Jones, J. Parsons, M. T. Kalichevsky-Dong, S. P. Palese, E. Cheung, and L. Dong, "Efficient 240W single-mode 1018nm laser from an Ytterbium-doped 50/400 μ m all-solid photonic bandgap fiber," *Opt. Express* **26**(3), 3138–3144 (2018).
23. C. Jauregui, H.-J. Otto, F. Stutzki, J. Limpert, and A. Tünnermann, "Simplified modelling the mode instability threshold of high power fiber amplifiers in the presence of photodarkening," *Opt. Express* **23**(16), 20203–20218 (2015).
24. R. Tao, P. Ma, X. Wang, P. Zhou, and Z. Liu, "Mitigating of modal instabilities in linearly-polarized fiber amplifiers by shifting pump wavelength," *J. Opt.* **17**(4), 045504 (2015).
25. J. W. Dawson, M. J. Messerly, R. J. Beach, M. Y. Shverdin, E. A. Stappaerts, A. K. Sridharan, P. H. Pax, J. E. Heebner, C. W. Siders, and C. P. J. Barty, "Analysis of the scalability of diffraction-limited fiber lasers and amplifiers to high average power," *Opt. Express*, **16**(17), 13240–13261 (2008).
26. M. Zervas, "Transverse mode instability, thermal lensing and power scaling in Yb³⁺-doped high-power fiber amplifiers," *Opt. Express*, **27**(13), 19019–19041 (2019).
27. J. T. Young, C. R. Menyuk, C. Wei, and J. Hu, "Increasing the power threshold in fiber amplifiers considering both the transverse mode and Brillouin instabilities," in *Proc. Conference on Lasers and Electro-Optics*, 3691159 (2022).
28. G. P. Agrawal *Nonlinear Fiber Optics* (Academic 2013).
29. A. Kobaykov, S. Kumar, D. Q. Chowdhury, A. B. Ruffin, M. Sauer, S. R. Bickham, and R. Mishra "Design concept for optical fibers with enhanced SBS threshold," *Opt. Express* **13**(14), 5338–5346 (2005).
30. D. Marcuse, *Theory of Dielectric Optical Waveguides* (Academic 1991).
31. C. R. Menyuk, J. T. Young, J. Hu, A. J. Goers, D. M. Brown, and M. L. Dennis, "Accurate and efficient modeling of the transverse mode instability in high energy laser amplifiers," *Opt. Express* **29**(12) 17746–17757 (2021).
32. G. W. Faris, L. E. Jusinski, and A. P. Hickman, "High-resolution stimulated Brillouin gain spectroscopy in glasses and crystals," *J. Opt. Soc. Am. B* **10**(4), 587–599 (1993).
33. E. P. Ippen, and R. H. Stolen, "Stimulated Brillouin scattering in optical fibers," *Appl. Phys. Lett.* **21**(11), 539–541 (1972).
34. R. W. Boyd, K. Rzaewski, and P. Narum, "Noise initiation of stimulated Brillouin scattering," *Phys. Rev. A*, **42**(9), 5514–5521 (1990).
35. J. Hu, B. S. Marks, Q. Zhang, and C. R. Menyuk, "Modeling backward-pumped Raman amplifiers," *J. Opt. Soc. Am. B*, **22**(10), 2083–2090, (2005).
36. F. Kong, C. Dunn, J. Parsons, M. T. Kalichevsky-Dong, T. W. Hawkins, M. Jones, and L. Dong, "Large-mode-area fibers operating near single-mode regime," *Opt. Express* **24**(10), 10295–10301 (2016).
37. N. Haarlamert, B. Sattler, A. Liem, M. Strecker, J. Nold, T. Schreiber, R. Eberhardt, A. Tünnermann, K. Ludewigt, and M. Jung, "Optimizing mode instability in low-NA fibers by passive strategies," *Opt. Lett.* **40**(10), 2317–2320 (2015).
38. D. Jain, Y. Jung, P. Barua, S. Alam, and J. K. Sahu, "Demonstration of ultra-low NA rare-earth doped step index fiber for applications in high power fiber lasers," *Opt. Express* **23**(6), 7407–7415 (2015).

39. C. Ye, J. Koponen, T. Kokki, J. Montiel-Ponsoda, A. Tervonen, and S. Honkanen, "Confined-doped ytterbium fibers for beam quality improvement: Fabrication and performance," *SPIE* **8237**, 823737 (2012).
40. H.-J. Otto, N. Modsching, C. Jauregui, J. Limpert, and A. Tünnermann, "Impact of photodarkening on the mode instability threshold," *Opt. Express* **23**(12), 15265–15277 (2015).
41. K.-H. Lee, K. Lee, Y. Kim, Y.-H. Cha, G. Lim, H. Park, H. Cho, and D.Y. Jeong, "Transverse mode instability induced by stimulated Brillouin scattering in a pulsed single-frequency large-core fiber amplifier," *Appl. Opt.* **54**(2), 189–194 (2015).